JACS Au
AN OPEN ACCESS JOURNAL OF THE AMERICAN CHEMICAL SOCIETY

pubs.acs.org/jacsau

Article

Metallophilic Interactions Drive Supramolecular Chirality Evolution and Amplify Circularly Polarized Luminescence

Ya-Jie Wang, Xiao-Yan Shi, Pengyao Xing,* and Shuang-Quan Zang*

Cite This: *JACS Au* 2023, 3, 565−574

Read Online

ACCESS | Metrics & More | Article Recommendations | Supporting Information

ABSTRACT: Metallophilic interactions, which are ubiquitous among d^{10} metal complexes with linear coordination geometries, can direct one-dimensional assembly. However, the ability of these interactions to manipulate chirality at the hierarchical level largely remains unknown. In this work, we unveiled the role of Au···Cu metallophilic interactions in directing the chirality of multicomponent assemblies. *N*-heterocyclic carbene−Au(I) complexes bearing amino acid residues formed chiral co-assemblies with $[CuI_2]^-$ anions via Au···Cu interactions. These metallophilic interactions changed the molecular packing modes of the co-assembled nanoarchitectures from lamellar to columnar chiral packing. This transformation initiated the emergence, inversion, and evolution of supramolecular chirality, thereby affording helical superstructures, depending on the geometry of building units. In addition, the Au···Cu interactions altered the luminescence properties and induced the emergence and amplification of circularly polarized luminescence. This work, for the first time, revealed the role of Au···Cu metallophilic interactions in modulating supramolecular chirality, paving the way for the construction of functional chiroptical materials based on d^{10} metal complexes.

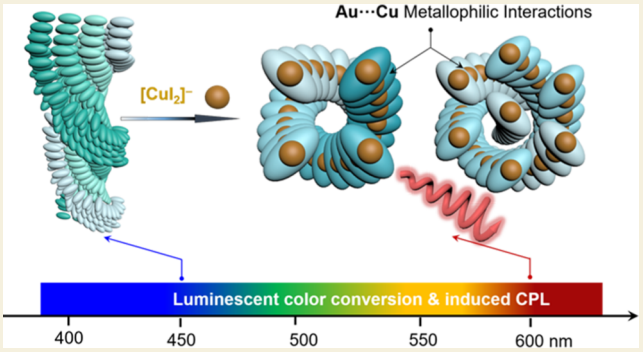

KEYWORDS: *metallophilic interactions, chirality, co-assembly, circularly polarized luminescence, N-heterocyclic carbene−Au(I) complexes*

INTRODUCTION

Chirality is a widespread phenomenon in nature exhibited by multifarious hierarchical structures ranging from the atomic to the macroscopic scales. Supramolecular chirality, which is defined as the spatially asymmetric packing of building blocks, has witnessed rapid development in fields such as chiroptical materials, sensing, detection, kinetic resolution, and information storage in the last decade.[1−4] Unlike the elaborate synthesis of inherently chiral molecular entities,[5] generating and controlling the supramolecular chirality of assemblies[6−15] based on flexible and dynamically manipulated noncovalent interactions and external fields are more facile and efficient. The methods for modulating the supramolecular chirality of assembled systems are generally divided into kinetic and thermodynamic protocols. These protocols utilize environmental factors (such as the solvent and temperature) and molecular topological design (such as functional groups) to influence the generation and variation of supramolecular chirality.[16] Compared with kinetic control, thermodynamic control of the supramolecular chirality of multicomponent assemblies is emerging.[17] The evolution of the supramolecular chirality of hierarchical co-assemblies by manipulation of dynamic inter-constituent forces, such as electrostatic, hydrogen bond, halogen bond, $\pi-\pi$ stacking, and charge-transfer interactions, has been investigated extensively in recent years.[18−22]

Metallophilic interactions are based on the propensities of d^8 and d^{10} transition metal ions, such as Pt(II), Au(I), Ag(I), and Cu(I), which are enhanced by the relativistic effect and electron correction of the closed-shell constituents.[23−29] Although metallophilic interactions are repulsive in nature, Pauli repulsion is suppressed by the linear coordination geometries of the d^{10} metal complexes. This leads to a close M···M distance that is shorter than the sum of the van der Waals radius. Thus, metallophilic interactions behave as attractive interactions with an order-of-magnitude strength similar to that of hydrogen bonds.[30] By tuning metallophilic interactions, numerous supramolecular materials with tailored properties have been constructed for diverse applications such as optoelectronics and catalysis. Owing to the chemical stability and coordination versatility of *N*-heterocyclic carbene (NHC) ligands, various chiral NHC−metal complexes have

Received: December 1, 2022
Revised: December 22, 2022
Accepted: January 4, 2023
Published: January 20, 2023

https://doi.org/10.1021/jacsau.2c00653
JACS Au 2023, 3, 565−574

Scheme 1. (a) Chemical Structures of Amino Acid-Derived $[Au(NHC)_2]^+I^-$ Complexes and (b) Schematic Representation of Helicity Inversion from Individual Self-Assembly to Co-Assembly with Columnar Chiral Packing

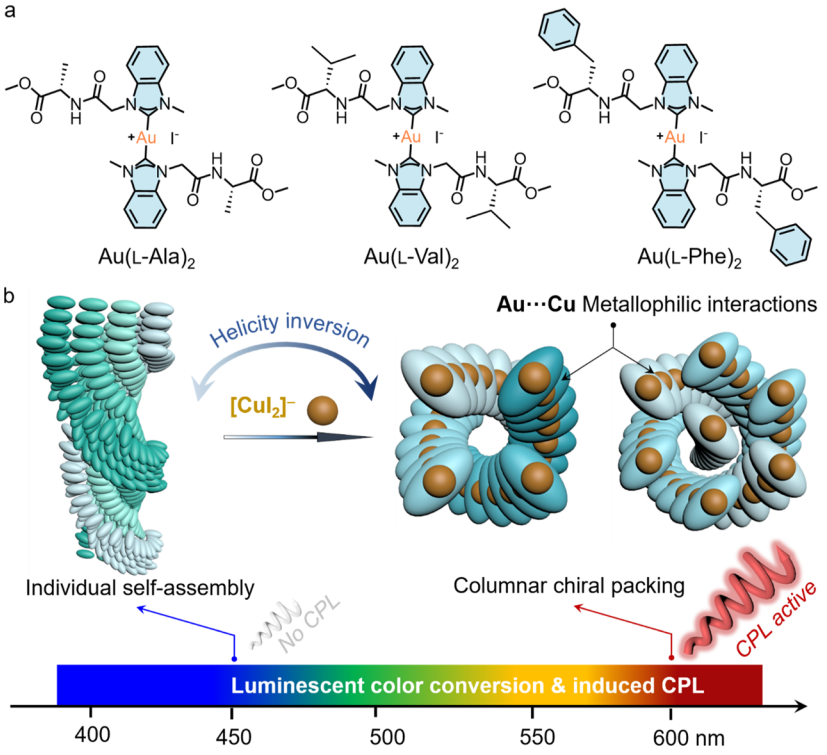

been synthesized.[31−33] For instance, Che et al. reported a series of NHC−gold (I) complex salts $[Au(NHC)_2][MX_2]$ (M = Au or Cu; X = halide, cyanide, or arylacetylide) consisting of alternating cations and anions arranged into one-dimensional (1D) chains. These further generated supramolecular polymers with tunable luminescence properties, in which the synergetic Au···M interactions and Coulombic attraction directed the co-assembly.[29,34−38] Among these complex salts, a pair of chiral $[Au(NHC)_2][Au(CN)_2]$ complex double salts displayed excitation-wavelength-dependent circularly polarized luminescence (CPL).[38] The tunable Au···Au distances were proven to be responsible for the tunable photoluminescence (PL). Au···Cu metallophilic interactions assisted by Coulombic attraction not only lead to strong binding energy[36] but also facilitate the formation of 1D structures. Thus, such metallophilic interactions are expected to be potential forces in manipulating the supramolecular chirality of nanoarchitectures in multicomponent systems. However, the role of Au···Cu metallophilic interactions in modulating chirality has not yet been revealed.

Herein, we introduced Au···Cu interactions to tune chiral self-assembly and chiroptical properties. Three enantiopure NHC−gold (I) complexes, $[Au(NHC)_2]^+I^-$, bearing diverse amino acid residues, including alanine (Ala), valine (Val), and phenylalanine (Phe), were synthesized as the model building blocks (Scheme 1a). $[CuI_2]^-$ ([18-Crown-6]-K^+ or [18C6]-K^+ as the counter cation)[35] was used as the anionic counterpart to co-assemble with the Au(I) complexes through the Au···Cu interactions with auxiliary Coulombic attraction. In solution, the least sterically hindered $Au(Ala)_2$ self-assembled into homochiral helically wound nanofibers. On the other hand, the other two complexes, $Au(Val)_2$ and $Au(Phe)_2$, produced achiral structures on nano- and microscales. Introducing $[CuI_2]^-$ through a co-precipitation protocol generated distinct co-assembled nanoarchitectures (Scheme 1b). $[CuI_2]^-$ was exclusively capable of modulating supramolecular chirality compared with the other anions used. Except in the case of the large sterically hindered $Au(Phe)_2$, integrating $[CuI_2]^-$ into the assemblies induced the formation of helical structures with inverted handedness, consistent with the chiroptical responses. The experimental and theoretical results indicated that the Au···Cu metallophilic interactions in the co-assemblies played a key role in directing the assembly arrays and caused a dramatic change in the molecular packing from lamellar stacking to columnar packing. In addition, the Au··Cu interactions induced luminescent color evolution and the emergence and amplification of CPL (Scheme 1). This work focused on the supramolecular chirality evolution of Au(I)-complex-based chiral assembly materials, exploring a pathway to fabricate chiroptical materials with modifiable handedness based on Au···Cu metallophilic interactions.

RESULTS AND DISCUSSION

Three amino-acid-derived NHC−Au(I) complexes ($[Au(NHC)_2]^+I^-$) formed co-assemblies with [18C6]-$K^+[CuI_2]^-$ via solution-processed bottom-up assembly. Aggregates of the three $[Au(NHC)_2]^+I^-$ complexes were obtained by evaporating the respective acetonitrile solutions. The co-assembly of the $[Au(NHC)_2]^+I^-$ complexes and [18C6]-$K^+[CuI_2]^-$ was triggered by co-precipitation in acetonitrile, followed by incubation and aging, under ambient conditions. The presence of cationic $[Au(NHC)_2]^+$ and anionic $[CuI_2]^-$ in the co-assemblies was confirmed by electrospray ionization−mass spectrometry in the positive and negative modes, respectively (Figures S1−S3). Both self- and co-assemblies were adequately studied by electron microscopy, circular dichroism (CD), thin-film powder X-ray diffraction (XRD), PL, and CPL.

https://doi.org/10.1021/jacsau.2c00653
JACS Au 2023, 3, 565−574

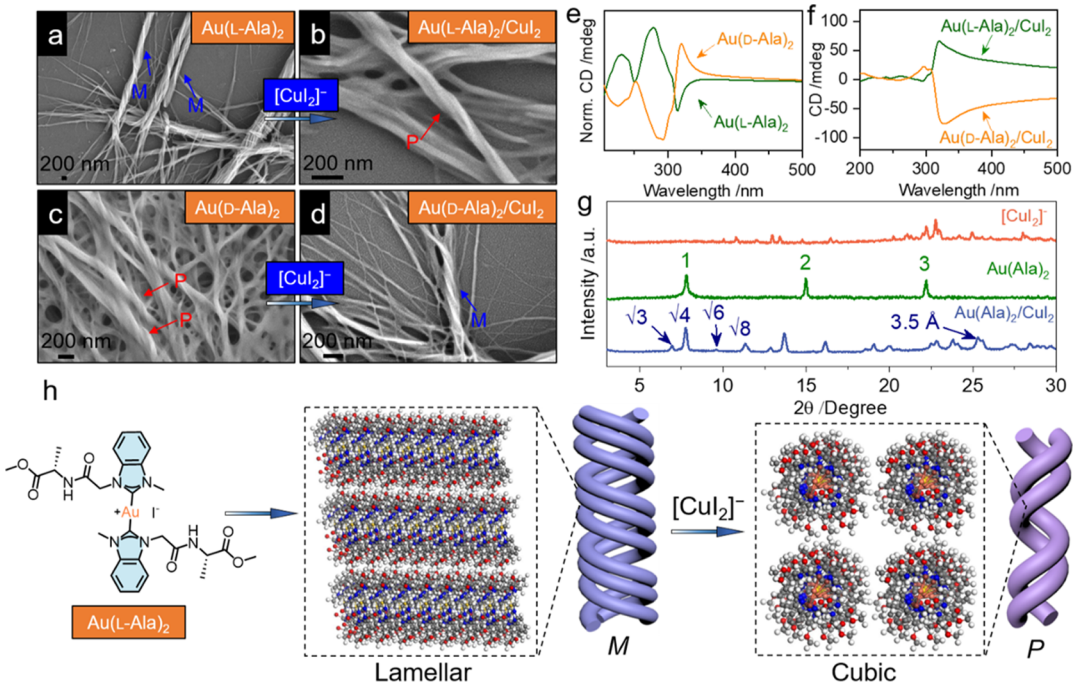

Figure 1. SEM images of (a,c) Au(L-Ala)$_2$ and Au(D-Ala)$_2$ self-assemblies and (b,d) their respective co-assemblies with $[CuI_2]^-$. CD spectral comparisons of (e) Au(L-Ala)$_2$ and Au(D-Ala)$_2$ self-assemblies and (f) their respective co-assemblies with $[CuI_2]^-$. (g) XRD pattern comparison of the individual self-assemblies and co-assemblies. (h) Schematic models of lamellar and cubic packing arrangements based on XRD results.

Because it has the least sterically hindered methyl group at the α-carbon position of the amino acid residue, Au(Ala)$_2$ was prioritized in the study. The self-assembly of Au(Ala)$_2$ produced twisted nanofibrous structures with a mean diameter of approximately 100 nm, as observed by scanning electron microscopy (SEM). As shown in Figures 1a and S4, the Au(L-Ala)$_2$ self-assembly displays *M*-handed homochirality, whereas *P*-chiral fibers are observed exclusively for the Au(D-Ala)$_2$ self-assembly (Figures 1c and S4). When Au(Ala)$_2$ co-assembled with $[CuI_2]^-$, similar fibrous structures were observed, albeit with reversed helicity. The *M*-type Au(L-Ala)$_2$ self-assembly changed to *P*-type fibers, and the *P*-chiral Au(D-Ala)$_2$ self-assembly converted to *M*-chiral helical fibers after co-assembly with $[CuI_2]^-$ (Figures 1b,d and S5).

This unique supramolecular chirality inversion was further supported by the CD spectra. The Au(Ala)$_2$ self-assembly featured a well-defined mirror Cotton effect at 230 nm resulting from the absolute chirality of the Ala residues. Moreover, a couple of exciton-type Cotton effects centered at approximately 310 nm were attributed to the aromatic groups (NHC). This result implies a chirality transfer from the amino acid residue to NHC and a shift from molecular chirality to supramolecular chirality (Figure 1e). This chirality transfer boosted the degree of polarization. The dissymmetry *g*-factor (g_{abs}), which reflects the polarization of absorbance, was calculated as $g_{abs} = \Delta\varepsilon/\varepsilon = \theta$ (mdeg)/(32,980 × Abs). In contrast to the negligible g_{abs} of Au(Ala)$_2$ in the solution state, a dramatic increase from 4.0×10^{-4} to 1.1×10^{-2} was observed after self-assembly. This was magnified 27.5-fold because of the effective chirality transfer to the supramolecular scale (Figure S6). Introducing $[CuI_2]^-$ into the Au(Ala)$_2$ self-assembly clearly reversed the Cotton effects. The Au(L-Ala)$_2$/CuI$_2$ co-assembly exhibited a positive extended exciton band at approximately 320 nm, in contrast to the negative-then-positive exciton Cotton effects shown by the Au(L-Ala)$_2$ self-assembly. The same condition was observed for the Au(D-Ala)$_2$/CuI$_2$ co-assembly, which showed a negative band, in contrast to the positive-then-negative exciton band exhibited by the Au(D-Ala)$_2$ self-assembly (Figure 1f). Such inversion in the CD spectra corresponds well to the helical morphology transformation, confirming the supramolecular chirality inversion after the integration of $[CuI_2]^-$ into the Au(Ala)$_2$ self-assembly.

A physical insight into the effect of $[CuI_2]^-$ on the tuning of supramolecular chirality was further investigated. Based on the XRD pattern comparison (Figure 1g), the molecular packing of the aggregates evolved after the incorporation of $[CuI_2]^-$. The Au(Ala)$_2$ self-assembly showed strong diffraction peaks at 7.8, 15.0, and 22.2° with an approximate distance ratio of 1:1/2:1/3, corresponding to a lamellar structure with (100), (200), and (300) planes and a *d*-spacing of 1.13 nm. This *d*-spacing is approximately equal to the length of the Au(Ala)$_2$ molecule (1.30 nm), suggesting that the molecules are stacked in a layer-by-layer motif. However, the Au(Ala)$_2$/CuI$_2$ co-assembly showed a different XRD pattern than the Au(Ala)$_2$ self-assembly, implying that $[CuI_2]^-$ induced a different molecular packing model. For the Au(Ala)$_2$/CuI$_2$ co-assembly, the diffraction peaks at 6.92, 7.76, 9.62, and 11.32° with a ratio of $\sqrt{3}:\sqrt{4}:\sqrt{6}:\sqrt{8}$ corresponded to bicontinuous cubic packing with a *d*-spacing of 1.54 nm, which was larger than that of the lamellar structure of the Au(Ala)$_2$ self-assembly. As shown in Figure 1g, at around 25° of the co-assembly XRD patterns, it should be attributed to the regular arrangement of atomic levels in the co-assembled fibers, which corresponds to a Au···Cu distance of about 3.5 Å. Similar fine features have been previously observed in XRD patterns of the orderly packed Au_{25} cluster assembled nanoribbon.[39] Based on the above-mentioned results, the proposed packing motif evolution from the Au(Ala)$_2$ self-assembly to the Au(Ala)$_2$/CuI$_2$ co-assembly is shown in Figure 1h. The Au(Ala)$_2$ molecules self-

https://doi.org/10.1021/jacsau.2c00653
JACS Au 2023, 3, 565−574

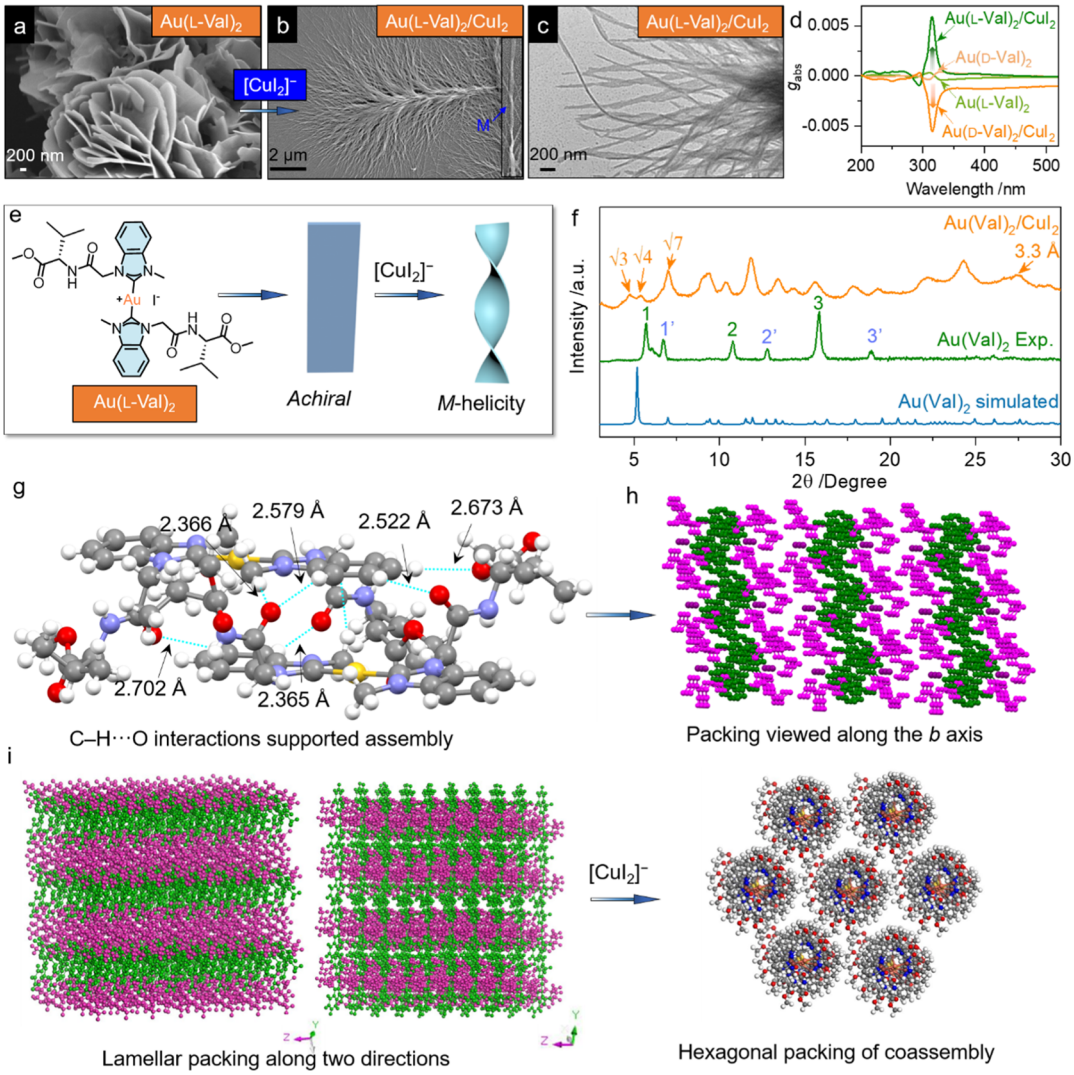

Figure 2. (a) SEM images of the Au(L-Val)$_2$ self-assembly. (b,c) SEM and TEM images of the Au(L-Val)$_2$ co-assembly with $[CuI_2]^-$. (d) Comparison of the g_{abs} values of the Au(L-Val)$_2$ and Au(D-Val)$_2$ self-assemblies and their co-assemblies with $[CuI_2]^-$. (e) Schematic representation of nanoscale chirality induced by $[CuI_2]^-$. (f) Comparison of XRD patterns simulated from the single-crystal data of the Au(L-Val)$_2$, individual self-assembly, and co-assembly. (g) Intermolecular interactions based on the X-ray crystal structure of Au(L-Val)$_2$. Arrows indicate the C−H···O interactions. (h) Packing viewed along the *b* axis of the crystal structure. (i) Simulated packing transformation induced by $[CuI_2]^-$ in the self-assembly scenario.

assemble into a lamellar microstructure and then become homochiral helical fibers based on the absolute chirality of the Ala residues. Previous studies of Au(NHC)$_2$/CuI$_2$ co-assemblies showed that consecutive Au···Cu interactions benefit the formation of 1D packing with alternating cationic $[Au(NHC)_2]^+$ and anionic $[CuI_2]^-$.[34,35] In the present Au(Ala)$_2$/CuI$_2$ co-assembly system, cationic $[Au(Ala)_2]^+$ and anionic $[CuI_2]^-$ units tended to pack alternately along the 1D direction on the periphery of the co-assembled arrays through Au···Cu interactions and then formed cubic sub-column structures accompanied by supramolecular chirality inversion compared with the Au(Ala)$_2$ self-assembly.

We further evaluated the influence of amino acid residues on the individual self-assemblies and co-assemblies. Unlike Au(Ala)$_2$, Au(Val)$_2$ possesses an isopropyl group at the α-carbon position of the amino acid residue, which may result in different self- and co-assembly behaviors. In contrast to the helical twisted nanofiber aggregates of Au(Ala)$_2$, stacked nanosheets on the microscale (Figures 2a and S7) were generated by the crystallization-induced self-assembly of Au(L-Val)$_2$. After the addition of 1 equiv of $[CuI_2]^-$ to the nanosheets, a gel phase was generated, transforming the co-assembly into twisted nanoribbons with a mean diameter of 50 nm, as observed by SEM and transmission electron microscopy (TEM) (Figures 2b,c and S7). *M*-handedness was observed for the Au(L-Val)$_2$/CuI$_2$ co-assembly. The morphological transformation between the Au(D-Val)$_2$ self-assembly and Au(D-Val)$_2$/CuI$_2$ co-assembly was similar to that of the corresponding L-enantiomers (Figure S8). Supramolecular chirality emerged through the co-assembly with $[CuI_2]^-$.

The generation and modulation of supramolecular chirality through the introduction of $[CuI_2]^-$ during the assembly process were investigated by CD characterization. A pair of well-defined mirror curves were obtained for the Au(Val)$_2$ self-assembly with an almost negligible g_{abs} of approximately 3×10^{-4}, indicative of the low degree of polarization of the absorption (Figure S9a). After incorporating $[CuI_2]^-$, strong Cotton effects centered at approximately 314 nm were

https://doi.org/10.1021/jacsau.2c00653
JACS Au 2023, 3, 565−574

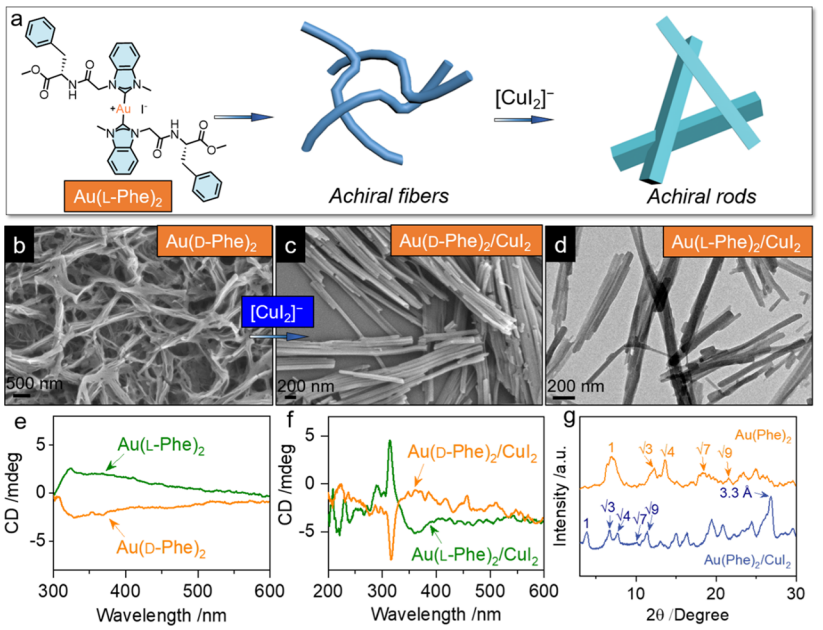

Figure 3. (a) Schematic representation of the morphological transformation of $Au(Phe)_2$ induced by $[CuI_2]^-$. SEM images of the (b) $Au(D\text{-}Phe)_2$ self-assembly and (c) $Au(D\text{-}Phe)_2/CuI_2$ co-assembly. (d) TEM images of the $Au(L\text{-}Phe)_2/CuI_2$ co-assembly. CD spectral comparisons of (e) $Au(L\text{-}Phe)_2$ and $Au(D\text{-}Phe)_2$ self-assemblies and (f) their respective co-assemblies with $[CuI_2]^-$. (g) XRD pattern comparison of the individual self-assemblies and co-assemblies.

observed (Figure S9b). The g_{abs} also increased up to 6×10^{-3}, which was 20-fold higher than that of the $Au(Val)_2$ self-assembly. This signifies that the emergence of supramolecular chirality is beneficial to the chiroptical properties (Figure 2d). Furthermore, similar to the $Au(Ala)_2$ self-assembly, introducing $[CuI_2]^-$ into the $Au(Val)_2$ self-assembly also achieved chirality inversion independent of the amino acid residue. As shown in Figure S9a, the $Au(L\text{-}Val)_2$ self-assembly features negative and positive exciton-type Cotton effects at approximately 314 nm, which are assigned to the NHC groups. When $[CuI_2]^-$ was integrated into the $Au(L\text{-}Val)_2$ self-assembly, the Cotton effect at 314 nm was inversed as a positive signal (Figure S9b). By varying the configuration from the L-to the D-enantiomer, the same CD signal variation occurred, confirming the negligible artifacts and validating the decisive effect of the absolute chirality on the guidance of the supramolecular chirality. However, in the solid states, the anisotropic effects are basically inevitable. In order to rule out the artifacts, we actually performed multiple tests to confirm the accuracy for both CD and CPL spectroscopy. Based on the above-mentioned results, incorporating $[CuI_2]^-$ into the $Au(Val)_2$ self-assembly enables the generation of supramolecular chirality to achieve chirality amplification and inversion.

The spontaneous self-assembly of $Au(L\text{-}Val)_2$ produced achiral nanosheets, while the introduction of $[CuI_2]^-$ generated supramolecular chirality with *M*-handedness (Figure 2e). To gain insights into the assembly mechanism of $Au(Val)_2$ and $Au(Val)_2/CuI_2$, single crystals of $Au(L\text{-}Val)_2$ were cultured through a liquid-phase diffusion protocol (dimethyl formamide vs diethyl ether), and XRD analysis was performed. The single-crystal structures exhibited C−H···O interactions between the $Au(L\text{-}Val)_2$ molecules, with distances of 2.365−2.702 Å, which are in the range of the reported hydrogen bond lengths (Figure 2g). The structure of the assembly supported by C−H···O interactions was characterized by a lamellar array along the *b* axis with alternately stacked $[Au(NHC)_2]^+$ units and amino acid residues (colored green and purple, respectively, shown in Figure 2h). Similar noncovalent C−H···O interactions might be present during the spontaneous aggregation, and the XRD pattern of the $Au(Val)_2$ self-assembly was different from that simulated using $Au(Val)_2$ single crystals (Figure 2f). This indicates that the solution-processed self-assembly adopts a distinct arrangement from that produced by thermodynamic crystallization. The XRD pattern of the $Au(Val)_2$ self-assembly showed two sets of peaks at 5.72, 10.78, and 15.84° (1, 2, 3) and 6.7, 12.8, and 18.82° (1′, 2′, 3′). This indicates the co-existence of two lamellar structures along two different directions with *d*-spacing values of 1.54 and 1.32 nm, in accordance with the size of the $Au(Val)_2$ molecules (1.60 and 1.31 nm from different directions). After co-assembly with $[CuI_2]^-$, an XRD pattern different from that of the individual self-assembly appeared. The main diffraction peaks of the $Au(Val)_2/CuI_2$ co-assembly were located at 4.78, 5.38, and 6.98° (approximate ratio of $\sqrt{3}:\sqrt{4}:\sqrt{7}$), corresponding to the (110), (200), and (210) planes of hexagonal columnar packing, respectively, with a *d*-spacing of 3.2 nm calculated from the Bragg equation. A relatively weaker peak at around 27° should be assigned as Au···Cu distance with about 3.3 Å. According to the above-mentioned results, the $Au(Val)_2$ self-assembly formed lamellar structures along two directions (Figure 2i). After incorporating $[CuI_2]^-$ into the assembly, the resulting co-assembly exhibited hexagonal packing, which further facilitated the assembly of a helical nanofibrous structure.

Owing to a larger sterically hindered benzyl group at the α-position, $Au(Phe)_2$ exhibited different self- and co-assembly behaviors compared with $Au(Ala)_2$ and $Au(Val)_2$ (Figure 3a). As shown in Figure 3b, $Au(D\text{-}Phe)_2$ self-assembles into slender fibrous structures, which then twist into thick fibers with an average diameter of approximately 250 nm without evident nanoscale chirality. Integrating $[CuI_2]^-$ into the assembly led to a morphological transformation from flexible fibers to rigid

https://doi.org/10.1021/jacsau.2c00653
JACS Au 2023, 3, 565−574

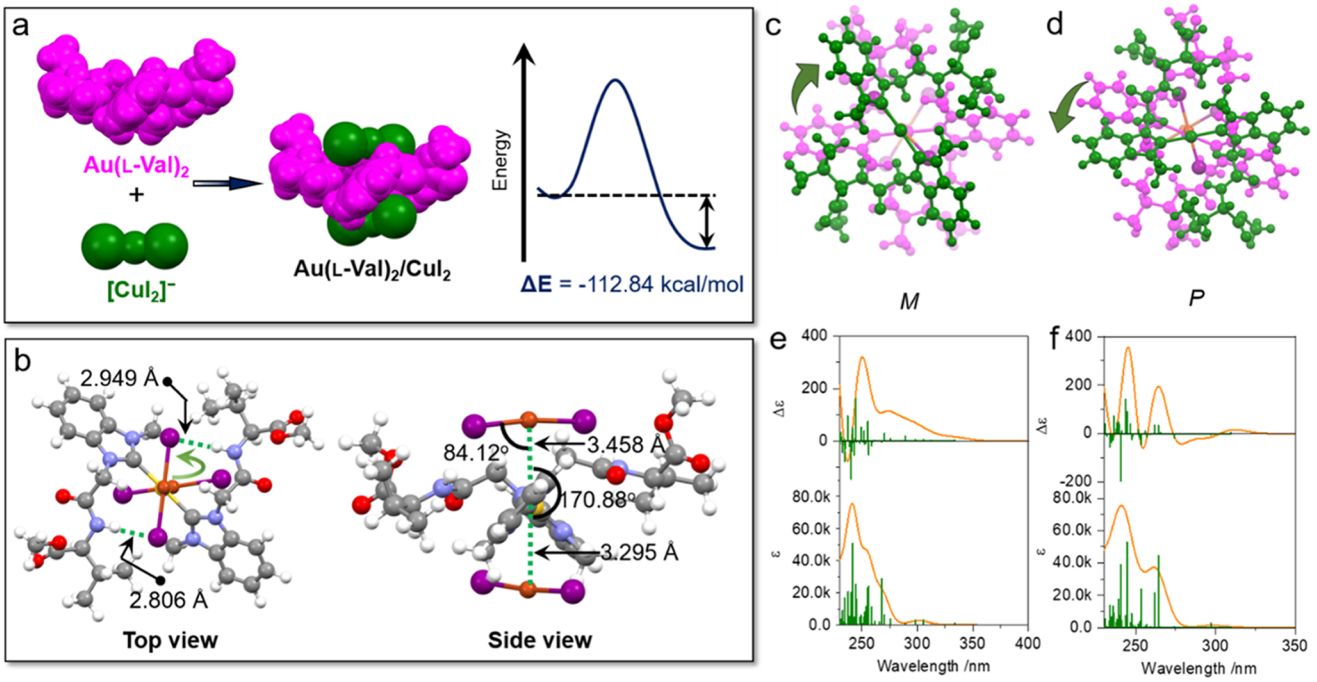

Figure 4. (a) Energy diagram of $Au(Val)_2/CuI_2$ co-assembly formation. (b) DFT-optimized structures of $Au(Val)_2/CuI_2$ at the B3LYP/def2-SVP level of theory. (c,f) DFT-optimized stacked structures and their corresponding calculated ECD spectra of the $Au(Val)_2/CuI_2$ co-assembly at the B3LYP/def2-SVP level of theory.

rods with a diameter of approximately 80 nm but without the generation of morphological supramolecular chirality (Figure 3c,d). The same situation also occurred in the $Au(L\text{-}Phe)_2$ self-assembly and $Au(L\text{-}Phe)_2/CuI_2$ co-assembly (Figure S10).

The CD signals of the $Au(Phe)_2$ and $Au(Phe)_2/CuI_2$ assemblies were also reversed, similar to those of the other two systems. As shown in Figure 3e, the CD spectra of the $Au(Phe)_2$ self-assembly with different configurations appear as well-defined mirror curves. The pair of extended bands centered at approximately 325 nm were positive for $Au(L\text{-}Phe)_2$ and negative for $Au(D\text{-}Phe)_2$. Incorporating $[CuI_2]^-$ into the $Au(Phe)_2$ self-assembly noticeably changed the Cotton effects (Figure 3f). The resultant $Au(Phe)_2/CuI_2$ co-assembly exhibited a couple of extended exciton-type Cotton effects at approximately 330 nm, with positive and negative bands for $Au(D\text{-}Phe)_2/CuI_2$, unlike the totally negative band for the $Au(D\text{-}Phe)_2$ self-assembly. Such behavior suggests that chirality inversion occurs after co-assembly with $[CuI_2]^-$.

The thin-film XRD patterns of the $Au(Phe)_2$ and $Au(Phe)_2/CuI_2$ assemblies were recorded to probe the molecular packing modes before and after the integration of $[CuI_2]^-$ (Figure 3g). The $Au(Phe)_2$ self-assembly displayed clear diffraction peaks at 6.88, 12.3, 13.64, 18.4, and 21.56° with an approximate ratio of $1{:}\sqrt{3}{:}\sqrt{4}{:}\sqrt{7}{:}\sqrt{9}$, corresponding to hexagonal columnar packing with a *d*-spacing of 1.28 nm. For the $Au(Phe)_2/CuI_2$ co-assembly, the XRD pattern showed a set of peaks at 3.88, 6.66, 7.58, 10.1, and 11.4° with the same approximate ratio, indicating the same hexagonal columnar packing, albeit with a larger *d*-spacing of 2.26 nm. Unlike the $Au(Phe)_2$ self-assembly, the co-assembly displayed a distinct peak at around 27°, which corresponded to a Au···Cu distance of about 3.3 Å. The above-mentioned phenomenon reveals that the introduction of $[CuI_2]^-$ into the $Au(Phe)_2$ self-assembly does not change the hexagonal columnar arrangement but stretches the assembled structure. Unlike the $Au(Ala)_2/CuI_2$ and $Au(Val)_2/CuI_2$ co-assemblies, the $Au(Phe)_2/CuI_2$ co-assembly possessing a large sterically hindered amino acid residue failed to generate morphological supramolecular chirality, indicating the effect of the substituents on the handedness of the assemblies. However, the integration of $[CuI_2]^-$ into the assembly also resulted in chirality inversion reflected in the chiroptical properties, further confirming the vital function of Au···Cu metallophilic interactions in manipulating chirality evolution.

To explore the Au···Cu metallophilic interactions within a co-assembly, density functional theory (DFT) calculations were performed on the $Au(L\text{-}Val)_2/CuI_2$ complex using the geometry extracted from the crystal structure. As shown in Figure 4a, the interaction energy (ΔE) between $Au(L\text{-}Val)_2$ and $[CuI_2]^-$ is $-112.84/2 = -56.42$ kcal/mol, which is comparable to the energy of an anion−cation $d^{10}\cdots d^{10}$ interaction, such as the Au···Au interaction.[36] Such a large binding energy indicates the strong binding affinity between $[Au(Val)_2]^+$ and $[CuI_2]^-$ due to the combined effects of the Au···Cu metallophilicity and the anion−cation and hydrogen bond interactions. The optimized structure of the $Au(L\text{-}Val)_2/CuI_2$ complex showed a sandwich construct with alternately stacked cationic $Au(L\text{-}Val)_2$ and anionic $[CuI_2]^-$. This arrangement is believed to be more favorable for supramolecular chiral packing along 1D growth. The Cu···Au···Cu torsion angle was 170.88°, which, being close to 180°, was beneficial for forming a 1D assembled structure (Figure 4b). The Au···Cu distances were 3.458 and 3.295 Å, which were comparable to the distances of $d^{10}\cdots d^{10}$ metallophilic interactions (especially Au···Cu interactions) reported in the literature.[34,35] Also, the Au···Cu distances obtained from the DFT calculations were consistent with the observations from the XRD patterns of the co-assemblies. In addition to the Au···Cu interactions, N−H···I hydrogen bonds were observed in the complex structure with bond lengths of 2.806 and 2.949 Å.

https://doi.org/10.1021/jacsau.2c00653
JACS Au 2023, 3, 565−574

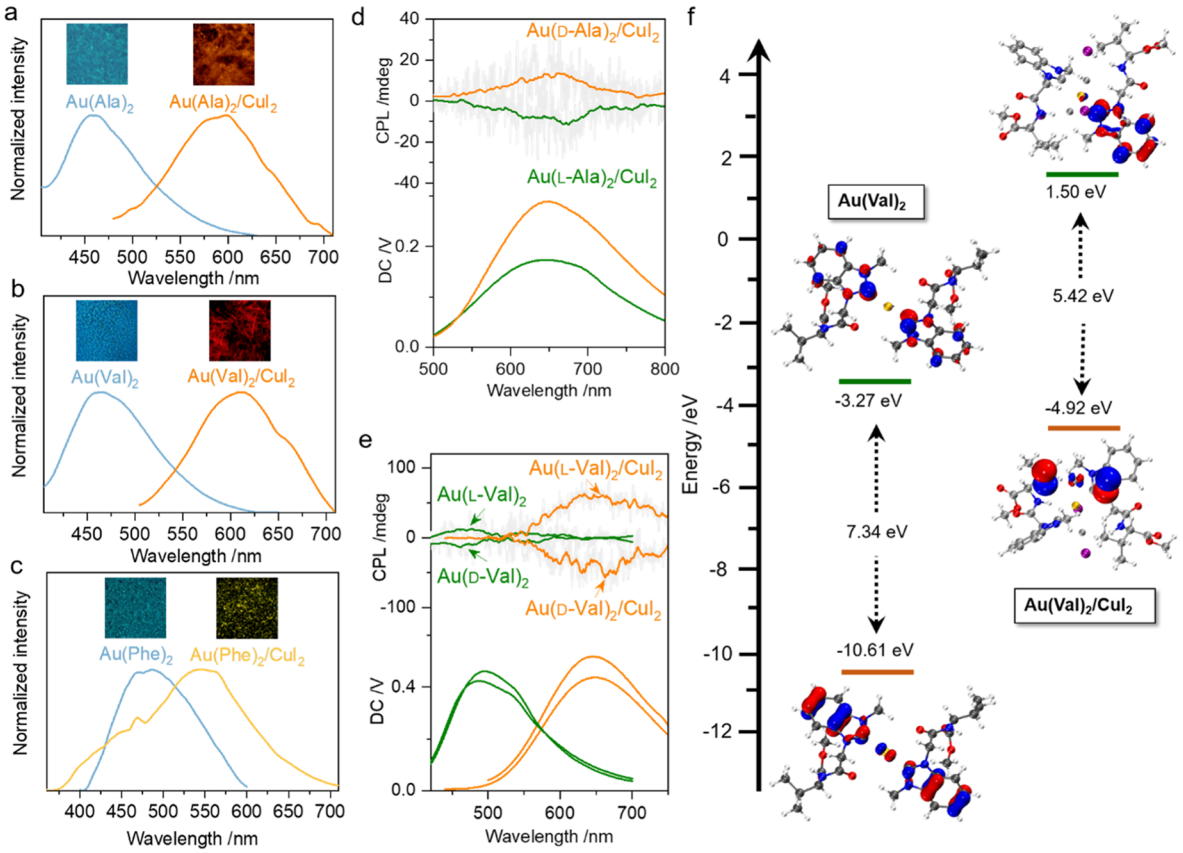

Figure 5. (a,b) Fluorescence spectra of the self- and co-assemblies. Insets show the luminescence colors of the corresponding systems observed by fluorescence microscopy. CPL spectra of the (c) $Au(Ala)_2/CuI_2$ co-assembly, (d) $Au(Val)_2$ self-assembly, and (e) $Au(Val)_2/CuI_2$ co-assembly. (f) HOMO−LUMO energy levels and the corresponding electron distribution maps of the $Au(Val)_2$ and $Au(Val)_2/CuI_2$ assemblies.

To investigate the correlation between supramolecular geometry and CD activity, electronic circular dichroism (ECD) calculations were performed. The $Au(L\text{-}Val)_2/CuI_2$ complex with optimized clockwise or anticlockwise screw sense was applied for the ECD calculations (Figure 4c−f). The $Au(L\text{-}Val)_2/CuI_2$ complex with a clockwise screw sense (*M*-handedness) displayed a positive Cotton effect in the range of 250−350 nm (Figure 4c,e) while that with the anticlockwise screw sense (*P*-handedness) afforded a positive-then-negative exciton Cotton effect at a wavelength of 300 nm (Figure 4d,f). The positive Cotton effect presented by the *M*-handed structure was consistent with the experimental CD spectra of the $Au(L\text{-}Val)_2/CuI_2$ co-assembly prepared by co-precipitation. This result indicates that the supramolecular chirality of the $Au(L\text{-}Val)_2/CuI_2$ co-assembly follows a clockwise *M*-handedness, which is in accordance with the observed morphology. Thus, the pivotal anion−cation Au···Cu interactions, assisted by the hydrogen bonds between $Au(L\text{-}Val)_2$ and $[CuI_2]^-$, guide the co-assembly structure and influence the helical direction of the supramolecular chirality.

The emergence of Au···Cu metallophilic interactions dramatically changed the PL properties of the Au(I) complexes. The fluorescence spectra of the self- and co-assemblies were measured, as shown in Figure 5a−c. The $[Au(NHC)_2]^+I^-$ complexes (NHC = Ala, Val, and Phe) displayed cyan emissions with major peaks centered at 456, 466, and 486 nm. After integration with $[CuI_2]^-$, the $Au(Ala)_2/CuI_2$ and $Au(Val)_2/CuI_2$ co-assemblies exhibited large emission shifts of up to 140 nm, while the emission shift of the $Au(Phe)_2/CuI_2$ co-assembly was 60 nm. The emission peaks of the $Au(NHC)_2/CuI_2$ (NHC = Ala, Val, and Phe) co-assemblies were 597, 612, and 546 nm, contributing to orange, red, and yellow luminescence, respectively, which was in good agreement with the luminescence images shown in Figure 5a−c. The decay profiles (Figure S11) showed that the emission lifetime of the self- and co-assemblies lasted for hundreds to thousands of nanoseconds, indicating phosphorescent emission.

The synergistic Au···Cu metallophilic interactions in the co-assemblies were assumed to facilitate supramolecular chirality and thus favor CPL emission. Samples of the self- and co-assemblies in the film state were used in the CPL tests, and the linear dichroism effect was excluded by repeated experiments. The CPL spectra of the $Au(Ala)_2$ and $Au(Phe)_2$ self-assemblies and $Au(Phe)_2/CuI_2$ co-assembly could not be obtained, possibly due to negligible luminescence dissymmetry factors (g_{lum}). In Figure 5d, $Au(L\text{-}Ala)_2/CuI_2$ and $Au(D\text{-}Ala)_2/CuI_2$ show right and left CPL, respectively. As the CPL spectrum represents the chirality in the photoexcited state while the CD spectrum reflects the chirality in the ground state, it is understandable that they are not consistent with each other owing to structural relaxation. The g_{lum} values were determined using the equation $g_{lum} = 2 \times [\text{ellipticity}/(32{,}980/\ln 10)]/\text{total}$ fluorescence intensity at the CPL maximum peak.[40] In addition, the g_{lum} of both the $Au(L\text{-}Ala)_2/CuI_2$ and $Au(D\text{-}Ala)_2/CuI_2$ co-assemblies was $\pm 7 \times 10^{-3}$ (Figure S12). For the $Au(L\text{-}Val)_2/CuI_2$ and $Au(D\text{-}Val)_2/CuI_2$ co-assemblies, CPL with a g_{lum} of $\pm$ 0.01 was obtained in contrast to the negligible

https://doi.org/10.1021/jacsau.2c00653
JACS Au 2023, 3, 565−574

CPL of the Au(L-Val)$_2$ and Au(D-Val)$_2$ self-assemblies (Figures 5e and S12). The chiroptical properties including CD and CPL originate from the differential absorption and emission of left- and right-handed circularly polarized light, which are determined by the screw sense of electronic transition dipole moments. In the self-assemblies, the point chirality of amino acids shall induce the helical orientation or packing of NHC-based chromophores, leading to the helical packing of transition dipole moments to afford chiroptical properties. With respect to this fact, the emergence of chiroptical properties is hardly associated with the scattering effect of light by the nanoscale assemblies. The CD and CPL extremum wavelengths correspond to the absorption and emission peaks of chromophores. The helical packing of chromophores in most cases is consistent with the helical sense observed using microscopic techniques such as SEM. The evolution behavior of the luminescence and chiroptical properties from self-assembly to co-assembly was caused by the Au···Cu metallophilic interactions. These interactions not only influenced the luminescence, leading to different degrees of bathochromic shift of the emission peaks, but also amplified the CPL to induce supramolecular chirality.

To gain insights into the correlation between the Au···Cu metallophilic interactions and lower-energy transitions of the co-assemblies, we performed time-dependent DFT calculations on the Au(L-Val)$_2$ and Au(L-Val)$_2$/CuI$_2$ assemblies using geometries extracted from the crystal structures. The resulting frontier orbitals are depicted in Figure 5f. The highest occupied molecular orbital (HOMO) and lowest unoccupied molecular orbital (LUMO) energy levels of Au(L-Val)$_2$ were −10.61 and −3.27 eV, respectively. The HOMO of the Au(L-Val)$_2$/CuI$_2$ complex was localized on the $[CuI_2]^-$ anions, with contribution from the Au···Cu interactions, with an energy of −4.92 eV. The LUMO was localized on the $[Au(NHC)]^+$ cations with an energy of 1.50 eV. Therefore, the low-lying electronic transitions can be described as ligand (anion)-to-ligand (cation) charge transfer mixed with Au···Cu interactions.[35] The narrower HOMO−LUMO energy gap (5.42 eV) of the co-assembly compared with that of the individual self-assembly (7.34 eV), which corresponds to the bathochromic emission, indicates the favorability of the co-assembly directed by Au···Cu metallophilic interactions with the assistance of Coulombic attraction. Thus, the theoretical calculations and experimental results confirm that Au···Cu metallophilic interactions play an important role in regulating the luminescence and chiroptical properties and the amplification of CPL emission.

CONCLUSIONS

In summary, we illustrated the modulation of supramolecular chirality via Au···Cu metallophilic interactions in co-assemblies of cationic NHC−Au(I) complexes and anionic $[CuI_2]^-$. The intrinsic aggregation of the $[Au(NHC)_2]^+I^-$ complexes varied with the steric size of the amino acid residue (Ala, Val, and Phe), producing different nanostructures such as helical nanofibers, stacked nanosheets, and thick fibers. After introducing $[CuI_2]^-$, the self-assembly structures transformed into helical packing, exhibiting supramolecular chirality for the Au(Ala)$_2$ and Au(Val)$_2$ self-assemblies. However, for the large sterically hindered Au(Phe)$_2$ self-assembly, morphological supramolecular chirality was not observed, although the chiroptical property was also inverted after co-assembly with $[CuI_2]^-$. The experimental and theoretical results indicated that the chiroptical and supramolecular chirality inversion and evolution were due to the changed molecular packing geometry directed by the Au···Cu metallophilic interactions. These interactions, assisted by Coulombic attraction, favored co-assembly and allowed the transformation to columnar chiral packing, which induced the inversion and emergence of a supramolecular chiral nanoarchitecture. Moreover, the Au···Cu metallophilic interactions also played an important role in the regulation of the luminescence properties and amplification of the CPL emission. Knowledge of the crucial function of Au···Cu metallophilic interactions in controlling supramolecular chirality in Au(NHC)$_2$/CuI$_2$ co-assemblies would guide the establishment of supramolecular chiral structures based on a reasonable choice of substituents. Thus, the findings of this work would facilitate the design and construction of functional chiroptical materials based on d^{10} metal complexes.

METHODS

Assembly Methods

Self-assembly was carried out by evaporating the solvent slowly. For example, 8.75 mg of Au(Ala)$_2$ was dispersed in 1 mL of acetonitrile and then spread on a quartz plate to form a film assembly. The co-assembly was prepared by a co-precipitation protocol. For the Au(Ala)$_2$/CuI$_2$ co-assembly system, Au(Ala)$_2$ (8.75 mg, 10 mmol) dispersed in acetonitrile (1 mL) and 18-Crown-6 K [CuI$_2$] (6.21 mg, 10 mmol) dispersed in acetonitrile (0.5 mL) were mixed and then co-precipitated to give a solid phase. For Au(Val)$_2$/CuI$_2$ and Au(Phe)$_2$/CuI$_2$ co-assembly systems, similar procedures were performed to afford gel and solid phases, respectively. All samples were aged under ambient conditions for at least 5 h before testing.

DFT Calculation Details

In order to gain insights into the metallophilic interactions in the co-assembly systems, the Au(L-Val)$_2$/CuI$_2$ system was selected as an example to be investigated according to the DFT calculations performed with the B3LYP-D3 (B3LYP with Grimme's DFT-D3 correction using zero-damping) functional using the Gaussian 16 suite of programs. A geometry of Au(L-Val)$_2$ extracted from the single-crystal XRD data combined with two optimized geometries of $[CuI_2]^-$ was used to construct a co-assembled structure and optimized using the B3LYP function and the def2-SVP basis set for all atoms. Coordinates were obtained from the above-mentioned optimized configuration for constructing molecular electrostatic potential maps (isodensity = 0.001 au). The single-point energy of Au(Val)$_2$ and $[CuI_2]^-$ and their counterpoise-corrected energy were calculated at the B3LYP/def2-TZVP level of theory. The interaction energy was computed as the difference in energy between the co-assembly and the sum of the energies of the individual components (equation below) and was corrected for basis set superposition error using the counterpoise technique. Interaction energy: $2E_{int} = E_{CO} - E_{Au} - 2E_{Cu}$, where E_{CO} = energy of the Au(Val)$_2$/CuI$_2$ co-assembly, E_{Au} = single-point energy of Au(Val)$_2$, and E_{Cu} = single-point energy of $[CuI_2]^-$.

ASSOCIATED CONTENT

Supporting Information

The Supporting Information is available free of charge at https://pubs.acs.org/doi/10.1021/jacsau.2c00653.

Materials, synthesis routes, experimental details, ^{1}H NMR spectra, ^{13}C NMR spectra, ESI−MS spectra, SEM images, CD spectra, time-resolved emission spectra, g_{lum} spectra, and crystal data tables (PDF)

X-ray single-crystal diffraction data of Au(L-Val)$_2$ (CIF)

https://doi.org/10.1021/jacsau.2c00653
JACS Au 2023, 3, 565−574

AUTHOR INFORMATION

Corresponding Authors

Pengyao Xing − *School of Chemistry and Chemical Engineering, Shandong University, Jinan 250100, People's Republic of China;* orcid.org/0000-0003-0487-2888; Email: xingpengyao@sdu.edu.cn

Shuang-Quan Zang − *Henan Key Laboratory of Crystalline Molecular Functional Materials, Henan International Joint Laboratory of Tumor Theranostical Cluster Materials, Green Catalysis Center, and College of Chemistry, Zhengzhou University, Zhengzhou 450001, People's Republic of China;* orcid.org/0000-0002-6728-0559; Email: zangsqzg@zzu.edu.cn

Authors

Ya-Jie Wang − *Henan Key Laboratory of Crystalline Molecular Functional Materials, Henan International Joint Laboratory of Tumor Theranostical Cluster Materials, Green Catalysis Center, and College of Chemistry, Zhengzhou University, Zhengzhou 450001, People's Republic of China*

Xiao-Yan Shi − *Henan Key Laboratory of Crystalline Molecular Functional Materials, Henan International Joint Laboratory of Tumor Theranostical Cluster Materials, Green Catalysis Center, and College of Chemistry, Zhengzhou University, Zhengzhou 450001, People's Republic of China*

Complete contact information is available at: https://pubs.acs.org/10.1021/jacsau.2c00653

Author Contributions

CRediT: **Ya-Jie Wang** conceptualization, formal analysis, funding acquisition, investigation, writing-original draft, writing-review & editing; **Xiao-Yan Shi** formal analysis, investigation; **Pengyao Xing** conceptualization, formal analysis, writing-review & editing; **Shuang-Quan Zang** conceptualization, funding acquisition, project administration, supervision, writing-review & editing.

Notes

The authors declare no competing financial interest.

ACKNOWLEDGMENTS

We gratefully acknowledge the financial support from the National Key R&D Program of China (2021YFA1200301), the National Natural Science Foundation of China (Nos. 92061201, 21825106, and 22205211), the Postdoctoral Research Grant in Henan Province (No. 202101001), and Zhengzhou University.

REFERENCES

(1) Liu, M.; Zhang, L.; Wang, T. Supramolecular Chirality in Self-Assembled Systems. *Chem. Rev.* **2015**, *115*, 7304−7397.

(2) Yashima, E.; Ousaka, N.; Taura, D.; Shimomura, K.; Ikai, T.; Maeda, K. Supramolecular Helical Systems: Helical Assemblies of Small Molecules, Foldamers, and Polymers with Chiral Amplification and Their Functions. *Chem. Rev.* **2016**, *116*, 13752−13990.

(3) Dong, J.; Liu, Y.; Cui, Y. Supramolecular Chirality in Metal−Organic Complexes. *Acc. Chem. Res.* **2021**, *54*, 194−206.

(4) Gong, Z.-L.; Li, Z.-Q.; Zhong, Y.-W. Circularly Polarized Luminescence of Coordination Aggregates. *Aggregate* **2022**, *3*, No. e177.

(5) Mori, T. Chiroptical Properties of Symmetric Double, Triple, and Multiple Helicenes. *Chem. Rev.* **2021**, *121*, 2373−2412.

(6) Zhang, L.; Qin, L.; Wang, X.; Cao, H.; Liu, M. Supramolecular Chirality in Self-Assembled Soft Materials: Regulation of Chiral Nanostructures and Chiral Functions. *Adv. Mater.* **2014**, *26*, 6959−6964.

(7) Huang, S.; Yu, H.; Li, Q. Supramolecular Chirality Transfer toward Chiral Aggregation: Asymmetric Hierarchical Self-Assembly. *Adv. Sci.* **2021**, *8*, 2002132.

(8) Peng, Q. C.; Luo, X. M.; Qin, Y. J.; Wang, T.; Bai, B.; Wei, X. L.; Li, K.; Zang, S. Q. Influence of Wallach's Rule on Chiral AIE Systems and Its Application in Cryptographic Information Storage. *CCS Chem.* **2022**, *4*, 3686−3692.

(9) Peng, Q.; Shuai, Z. Molecular Mechanism of Aggregation-Induced Emission. *Aggregate* **2021**, *2*, No. e91.

(10) Ma, S.; Du, S.; Pan, G.; Dai, S.; Xu, B.; Tian, W. Organic Molecular Aggregates: From Aggregation Structure to Emission Property. *Aggregate* **2021**, *2*, No. e96.

(11) Zhang, X.; Xu, Y.; Valenzuela, C.; Zhang, X.; Wang, L.; Feng, W.; Li, Q. Liquid Crystal-Templated Chiral Nanomaterials: From Chiral Plasmonics to Circularly Polarized Luminescence. *Light Sci. Appl.* **2022**, *11*, 233.

(12) Wang, L.; Urbas, A. M.; Li, Q. Nature-Inspired Emerging Chiral Liquid Crystal Nanostructures: From Molecular Self-Assembly to DNA Mesophase and Nanocolloids. *Adv. Mater.* **2020**, *32*, 1801335.

(13) Chen, X.-M.; Zhang, S.; Chen, X.; Li, Q. Tunable Circularly Polarized Luminescent Supramolecular Systems: Approaches and Applications. *ChemPhotoChem* **2022**, *6*, No. e202100256.

(14) He, Y.; Lin, S.; Guo, J.; Li, Q. Circularly Polarized Luminescent Self-organized Helical Superstructures: From Materials and Stimulus-Responsiveness to Applications. *Aggregate* **2021**, *2*, No. e141.

(15) Ye, Q.; Zheng, F.; Zhang, E.; Bisoyi, H. K.; Zheng, S.; Zhu, D.; Lu, Q.; Zhang, H.; Li, Q. Solvent Polarity Driven Helicity Inversion and Circularly Polarized Luminescence in Chiral Aggregation Induced Emission Fluorophores. *Chem. Sci.* **2020**, *11*, 9989−9993.

(16) Dou, X.; Mehwish, N.; Zhao, C.; Liu, J.; Xing, C.; Feng, C. Supramolecular Hydrogels with Tunable Chirality for Promising Biomedical Applications. *Acc. Chem. Res.* **2020**, *53*, 852−862.

(17) Xing, P.; Zhao, Y. Controlling Supramolecular Chirality in Multicomponent Self-Assembled Systems. *Acc. Chem. Res.* **2018**, *51*, 2324−2334.

(18) Wang, F.; Ji, W.; Yang, P.; Feng, C.-L. Inversion of Circularly Polarized Luminescence of Nanofibrous Hydrogels through Co-assembly with Achiral Coumarin Derivatives. *ACS Nano* **2019**, *13*, 7281−7290.

(19) An, S.; Hao, P.; Xing, P. Halogen Bonding Mediated Hierarchical Supramolecular Chirality. *ACS Nano* **2021**, *15*, 15306−15315.

(20) Liu, G.; Sheng, J.; Teo, W. L.; Yang, G.; Wu, H.; Li, Y.; Zhao, Y. Control on Dimensions and Supramolecular Chirality of Self-Assemblies through Light and Metal Ions. *J. Am. Chem. Soc.* **2018**, *140*, 16275−16283.

(21) Martial, B.; Lefèvre, T.; Buffeteau, T.; Auger, M. Vibrational Circular Dichroism Reveals Supramolecular Chirality Inversion of α-Synuclein Peptide Assemblies upon Interactions with Anionic Membranes. *ACS Nano* **2019**, *13*, 3232−3242.

(22) Ji, J.; Wei, X.; Wu, W.; Fan, C.; Zhou, D.; Kanagaraj, K.; Cheng, G.; Luo, K.; Meng, X.-G.; Yang, C. The More the Slower: Self-Inhibition in Supramolecular Chirality Induction, Memory, Erasure, and Reversion. *J. Am. Chem. Soc.* **2022**, *144*, 1455−1463.

(23) Yam, V. W.-W.; Au, V. K.-M.; Leung, S. Y.-L. Light-Emitting Self-Assembled Materials Based on d^8 and d^{10} Transition Metal Complexes. *Chem. Rev.* **2015**, *115*, 7589−7728.

(24) Katz, M. J.; Sakai, K.; Leznoff, D. B. The Use of Aurophilic and Other Metal−Metal Interactions as Crystal Engineering Design Elements to Increase Structural Dimensionality. *Chem. Soc. Rev.* **2008**, *37*, 1884−1895.

(25) Pyykkö, P. Strong Closed-Shell Interactions in Inorganic Chemistry. *Chem. Rev.* **1997**, *97*, 597−636.

(26) Schmidbaur, H.; Schier, A. Aurophilic Interactions as a Subject of Current Research: An Up-Date. *Chem. Soc. Rev.* **2012**, *41*, 370−412.
(27) Schmidbaur, H.; Schier, A. Argentophilic Interactions. *Angew. Chem., Int. Ed.* **2015**, *54*, 746−784.
(28) Harisomayajula, N. V. S.; Makovetskyi, S.; Tsai, Y.-C. Cuprophilic Interactions in and between Molecular Entities. *Chem.—Eur. J.* **2019**, *25*, 8936−8954.
(29) Chen, Y.; Cheng, G.; Li, K.; Shelar, D. P.; Lu, W.; Che, C.-M. Phosphorescent Polymeric Nanomaterials with Metallophilic $d^{10}\cdots d^{10}$ Interactions Self-Assembled from $[Au(NHC)_2]^+$ and $[M(CN)_2]^-$. *Chem. Sci.* **2014**, *5*, 1348−1353.
(30) Wan, Q.; Yang, J.; To, W.-P.; Che, C.-M. Strong Metal−Metal Pauli Repulsion Leads to Repulsive Metallophilicity in Closed-Shell d^8 and d^{10} Organometallic Complexes. *Proc. Natl. Acad. Sci. U.S.A.* **2021**, *118*, No. e2019265118.
(31) Wang, F.; Liu, L.; Wang, W.; Li, S.; Shi, M. Chiral NHC−Metal-Based Asymmetric Catalysis. *Coord. Chem. Rev.* **2012**, *256*, 804−853.
(32) Deng, M.; Mukthar, N. F. M.; Schley, N. D.; Ung, G. Yellow Circularly Polarized Luminescence from C_1-Symmetrical Copper(I) Complexes. *Angew. Chem., Int. Ed.* **2020**, *59*, 1228−1231.
(33) Ying, A.; Ai, Y.; Yang, C.; Gong, S. Aggregation-Dependent Circularly Polarized Luminescence and Thermally Activated Delayed Fluorescence from Chiral Carbene-Cu^I-Amide Enantiomers. *Angew. Chem., Int. Ed.* **2022**, *61*, No. e202210490.
(34) Cao, Y.; Yang, J.-G.; Deng, Y.; Wang, S.; Liu, Q.; Shen, C.; Lu, W.; Che, C.-M.; Chen, Y.; He, L. Amine-Responsive Disassembly of Au^I−Cu^I Double Salts for Oxidative Carbonylation. *Angew. Chem., Int. Ed.* **2020**, *59*, 2080−2084.
(35) Liu, Q.; Xie, M.; Chang, X.; Cao, S.; Zou, C.; Fu, W.-F.; Che, C.-M.; Chen, Y.; Lu, W. Tunable Multicolor Phosphorescence of Crystalline Polymeric Complex Salts with Metallophilic Backbones. *Angew. Chem., Int. Ed.* **2018**, *57*, 6279−6283.
(36) Liu, Q.; Xie, M.; Chang, X.; Gao, Q.; Chen, Y.; Lu, W. Correlating Thermochromic and Mechanochromic Phosphorescence with Polymorphs of a Complex Gold(I) Double Salt with Infinite Aurophilicity. *Chem. Commun.* **2018**, *54*, 12844−12847.
(37) Da, X.; Yu, F.-H.; Zhang, C.; Wang, Z.; Jian, Y.; Hou, Y.; Chen, Y.; Wang, X.; Zhou, Q. A Bioorthogonal Assembly Based on Metallophilic Interactions for Selective Imaging and PDT Treatment of Cancer Cells. *Inorg. Chem. Front.* **2022**, *9*, 2290−2297.
(38) Yang, J.-G.; Li, K.; Wang, J.; Sun, S.; Chi, W.; Wang, C.; Chang, X.; Zou, C.; To, W.-P.; Li, M.-D.; Liu, X.; Lu, W.; Zhang, H.-X.; Che, C.-M.; Chen, Y. Controlling Metallophilic Interactions in Chiral Gold(I) Double Salts towards Excitation Wavelength-Tunable Circularly Polarized Luminescence. *Angew. Chem., Int. Ed.* **2020**, *59*, 6915−6922.
(39) Wu, Z.; Du, Y.; Liu, J.; Yao, Q.; Chen, T.; Cao, Y.; Zhang, H.; Xie, J. Aurophilic Interactions in the Self-Assembly of Gold Nanoclusters into Nanoribbons with Enhanced Luminescence. *Angew. Chem., Int. Ed.* **2019**, *58*, 8139−8144.
(40) Yang, D.; Duan, P.; Zhang, L.; Liu, M. Chirality and Energy Transfer Amplified Circularly Polarized Luminescence in Composite Nanohelix. *Nat. Commun.* **2017**, *8*, 15727.

https://doi.org/10.1021/jacsau.2c00653
JACS Au 2023, 3, 565−574